Many-electron effective potential in low-dimensional nanostructures: Towards understanding the Wigner crystallization

Reyna Méndez-Camacho,[1,2,*] Esteban Cruz-Hernández,[1] and Ramón Castañeda-Priego[2,†]

[1]*Coordinación para la Innovación y Aplicación de la Ciencia y la Tecnología, Universidad Autónoma de San Luis Potosí, Sierra Leona 550, 78210 San Luis Potosí, México*

[2]*División de Ciencias e Ingenierías, Campus León, Universidad de Guanajuato, Loma del Bosque 103, 37150 León, México*

(Received 4 February 2019; revised manuscript received 5 July 2019; published 29 August 2019)

We present the derivation and application of an analytical effective potential that is able to describe, in a simple way, the interaction of many electrons confined in low-dimensional structures of realistic size. The effective potential takes into account the contribution of both the electron-electron interaction inside the nanostructure and the quantum confinement by a surrounding material. With this model, we explore the electronic distribution in quantum wells, wires, and dots in the full range from doped to high-doped concentrations. We also use this effective potential to explicitly determine the parameters that trigger the formation of the Wigner molecule in quantum wires. The comparison with experimental data reported in the literature shows the accuracy and reliability of this potential model.

DOI: 10.1103/PhysRevB.100.085438

I. INTRODUCTION

The strong confinement of electrical carriers, photons, and/or phonons in nanostructures can trigger unique physical phenomena that make those structures very attractive experimental systems with great potential applications in nanotechnology [1,2]. Currently, by means of different growth techniques such as hydride vapor phase epitaxy, metal-organic chemical-vapor deposition, and molecular-beam epitaxy, high-quality nanostructures of a wide range of materials, geometries, and doping levels can be synthesized [3–5].

Among the most fundamental and interesting questions observed in nanostructures are those related to the collective effect of electron-electron (*e-e*) interactions and quantum confinement [6–14]. One remarkable example where the competition between many-body forces and spatial restrictions leads to interesting phenomena is the Wigner crystallization; under specific conditions electrons spontaneously form a self-organized lattice in quantum wires (QWRs) [15–19].

When many-body interactions are explicitly included in the modeling of nanostructures, usually, long computational times and complex mathematical calculations are required to deal with realistic electronic densities and the nanometric or even micrometric size of the structures [10,13,20–24]. For that reason, in spite of the fundamental importance of the interaction of many electrons in the collective phenomena, the contribution of this interaction to the formation of new structures, such as the Wigner crystal, has remained a relatively unexplored field.

Recently, we proposed a simple approach to deal with the problem of many electrons confined in semiconductor QWRs by numerically solving the Schrödinger equation of two nonrelativistic electrons without spin, confined in square QWRs of infinite barriers and interacting effectively through a Yukawa-like potential [25]. In that work, the use of the Yukawa potential allowed us to study the interaction of a large number of electrons just by selecting a screening parameter κ [25]. However, one of the main limitations to its application is the fact that the confinement effects produced by the nanometric cross section of the QWRs are not explicitly included in the model.

In this contribution, we derive an analytical effective potential that is able to describe the *e-e* interaction, via a Yukawa-like potential, as well as the confinement in all three spatial dimensions. The reliability of this effective potential is investigated by its comparison with the Yukawa approach [25] and with experimental observations of the Wigner crystallization in QWRs reported elsewhere [13,14].

II. EFFECTIVE POTENTIAL: DERIVATION AND SOME FEATURES

A. Analytical derivation

For the derivation of the effective potential, a system of electrons confined to a square GaAs structure embedded in a matrix of $Al_xGa_{1-x}As$ (see Fig. 1) was considered. In such a system, the two-electron Hamiltonian is given by [25]

$$H = -\frac{\hbar^2}{2m_e^*}\nabla_i^2 + V_{\text{e-w}} + V_Y(r_{12}), \tag{1}$$

where $i = 1, 2$ accounts for the two electrons, $\hbar \equiv h/2\pi$, h is the Planck constant, m_e^* is the effective electron mass, and $V_{\text{e-w}}$ is the electron-wall potential in the x-y plane. The *e-e* interaction was considered to have the form of a Yukawa-like potential $V_Y(r_{12})$ [26]. This approach is similar to the well-known jellium model typically employed in solid-state physics, but with the difference that we consider two

*reyna.mendez@uaslp.mx
†ramoncp@fisica.ugto.mx

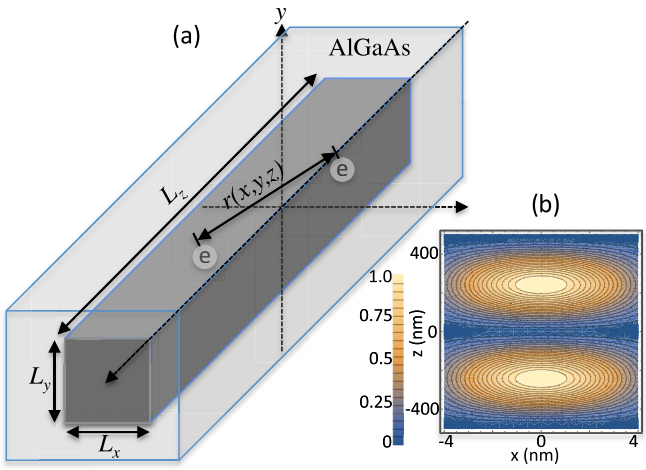

FIG. 1. (a) Schematic representation of two electrons separated by a distance r, located in a rectangular GaAs structure of length L_z and cross section $L_x \cdot L_y$ and embedded in a matrix of AlGaAs, and (b) x-z contour plot, obtained from the effective potential, Eq. (21), for $L_x = L_y = 8$ nm, $L_z = 1\,\mu$m, and $n = 10^{18}$ e/cm^3. The plot shows the test and screening electron distribution inside the GaAs matrix. For this small cross-sectional size, a fraction of the electronic distribution is able to tunnel into the x-y AlGaAs barrier.

indistinguishable "test" electrons immersed in a homogeneous electronic density (the "screening" electrons). However, it is worth noting that there is not a real distinction between the (test) electrons that interact through the Yukawa-like potential and the virtual (screening) electrons that take part in the screening process. So the results do reflect the behavior of the electronic density inside the heterostructures. Note that in the literature, the Yukawa-like potential goes by different names depending on the system under study, for example, the Debye-Hückel potential [27] in plasma physics and the Thomas-Fermi potential [28,29] for atomic systems. This potential is of particular interest because a simple variation of the screening parameter κ allows one to modify the electronic density, ranging from the bare Coulomb regimen (just two electrons) up to high-doped semiconductor structures (of the order of $10^{23}\,e/\text{cm}^3$). Such a potential has the following mathematical form [25]:

$$V_Y(r_{12}) = \frac{e^2}{4\pi\epsilon}\frac{\exp\left[-\kappa r_{12}\right]}{r_{12}}, \tag{2}$$

where $\epsilon = \epsilon_0\epsilon_r$, ϵ_0 is the vacuum permittivity, ϵ_r is the dielectric constant of the material, r_{12} is the e-e separation distance $\sqrt{(x_1-x_2)^2+(y_1-y_2)^2+(z_1-z_2)^2}$, and κ is the Debye-Hückel screening parameter, given by [30]

$$\kappa = \sqrt{\frac{2e^2 n}{\epsilon k_B T}}, \tag{3}$$

with n being the electronic density, k_B being the Boltzmann constant, and T being the absolute temperature. It is worth noting that the Yukawa form assumed here is strictly correct for three-dimensional screening or if both the longitudinal and lateral dimensions of the system are significantly larger than the screening length, defined by κ^{-1}. In this work, we report only electronic concentrations and geometries where the latest conditions are fulfilled.

If the contribution to the total energy of the system due to the x-y quantum confinement becomes significantly larger than the Yukawa interaction, which is the case for $L_{x,y} \lesssim 30$ nm in a GaAs nanostructure, the Yukawa contribution can be considered a small perturbation in the x and y components [31]. As a consequence, the transversal ($\perp$) and longitudinal ($\parallel$) contributions of Eq. (1) can be split as follows:

$$H_\perp(x,y) = -\frac{\hbar^2}{2m_e^*}\left(\frac{\partial^2}{\partial x_1^2}+\frac{\partial^2}{\partial x_2^2}+\frac{\partial^2}{\partial y_1^2}+\frac{\partial^2}{\partial y_2^2}\right)+V_{\text{e-w}}(x,y), \tag{4}$$

which represents the confinement due to the walls in the transversal x-y section, and

$$H_\parallel(z) = -\frac{\hbar^2}{2m_e^*}\left(\frac{\partial^2}{\partial z_1^2}+\frac{\partial^2}{\partial z_2^2}\right)+\frac{e^2}{4\pi\epsilon}\frac{e^{-\kappa r_{12}}}{r_{12}}, \tag{5}$$

which considers the confinement along the z axis. The confinement along the z direction is included in the calculation of $\Psi_\parallel(z)$ by means of the boundary conditions at $\pm L_z/2$, which is equivalent to considering infinite barriers at those L_z edges.

The e-e interaction energy can be written in an integral representation as

$$W = \int d^3r_1 d^3r_2\left(\frac{e^2}{4\pi\epsilon}\frac{e^{-\kappa r_{12}}}{r_{12}}\right)|\Psi(\vec{r})|^2. \tag{6}$$

Then, if the transversal and longitudinal components of the wave function are separated as

$$\Psi(\vec{r}) = \psi_\perp(x_1,y_1)\psi_\perp(x_2,y_2)\psi_\parallel(z_1,z_2), \tag{7}$$

the ground-state wave function $\psi_\perp(x,y)$ can be calculated from the Schrödinger equation for Eq. (4) as

$$\psi_\perp(x,y) = N_x N_y \cos(lx)\cos(ly), \tag{8}$$

with

$$l = \sqrt{\frac{2m_e^*}{\hbar^2}E_{0\text{-}j}}, \tag{9}$$

where $E_{0-j} \equiv E_{x,y}$ is the energy of the ground state in the x-y plane, with $j = x$ or y, and N_x and N_y are normalization constants.

In order to derive the effective potential, we consider the Fourier transform of $\psi_\perp^2(x,y)$, denoted by $G_{\psi_\perp}(q_x,q_y)$ and given by

$$\psi_\perp^2(x,y) = \frac{1}{(2\pi)^2}\int dq_x dq_y G_{\psi_\perp}(q_x,q_y)e^{-i(q_x x+q_y y)}, \tag{10}$$

where $\vec{q}$ is the wave number vector and

$$G_{\psi_\perp}(q_x,q_y) = \frac{\pi}{2}N_x^2[\delta(q_x)+\delta(q_x-l)+\delta(q_x+l)] \times N_y^2[\delta(q_y)+\delta(q_y-l)+\delta(q_y+l)]. \tag{11}$$

On the other hand, the longitudinal component can be written for some $G_{\psi_\parallel}(q_z)$ as

$$\psi_\parallel^2(z) = \frac{1}{(2\pi)^2}\int dq_z G_{\psi_\parallel}(q_z)e^{-i(q_z z)}, \tag{12}$$

and the Yukawa potential can be expressed in terms of its Fourier transform as

$$\frac{e^{-\kappa r_{12}}}{r_{12}} = \frac{1}{2\pi^2}\int d^3q \frac{e^{-i(q_x x+q_y y+q_z z)}}{\kappa^2+q_x^2+q_y^2+q_z^2}. \tag{13}$$

Then, by placing Eqs. (7), (10), (12), and (13) into Eq. (6), the next expression for the *e*-*e* interaction energy can be obtained:

$$W = \frac{e^2}{4\pi\epsilon 2^7\pi^8}\int d^3r\int d^3q \frac{G_{\psi_\perp}^2(q_x,q_y)G_{\psi_\parallel}(q_z)}{\kappa^2+q_x^2+q_y^2+q_z^2} \times e^{-i(q_x x+q_y y+q_z z)}, \tag{14}$$

where $d^3q \equiv dq_x dq_y dq_z$ and $d^3r \equiv dxdydz$. Integrating over r,

$$W = \frac{e^2}{4\pi\epsilon 2\pi^2}\int d^3q \frac{G_{\psi_\perp}^2(q_x,q_y)G_{\psi_\parallel}(q_z)}{\kappa^2+q_x^2+q_y^2+q_z^2}. \tag{15}$$

Now, as

$$G_{\psi_\parallel}(q_z) = \int dz\psi_\parallel^2(z)e^{i(q_z z)}, \tag{16}$$

Eq. (15) can thus be expressed as

$$W = \frac{e^2}{4\pi\epsilon 2\pi^2}\int dz d^3q \frac{G_{\psi_\perp}^2(q_x,q_y)\psi_\parallel^2(z)e^{i(q_z z)}}{\kappa^2+q_x^2+q_y^2+q_z^2}. \tag{17}$$

Then, by using the equality

$$\int_{-\infty}^{\infty} dq_z \frac{e^{iq_z z}}{q_x^2+q_y^2+q_z^2+\kappa^2} = \frac{\pi e^{-|z|\sqrt{q_x^2+q_y^2+\kappa^2}}}{\sqrt{q_x^2+q_y^2+\kappa^2}}, \tag{18}$$

Eq. (17) can be rewritten as

$$W = \frac{1}{2\pi}\int_{-\infty}^{\infty} dz\psi_\parallel^2(z_1,z_2)V_{\text{eff}}(z_1,z_2), \tag{19}$$

where V_{eff} has been defined as

$$V_{\text{eff}}(z) = \frac{e^2}{4\pi\epsilon}\int_l^{\infty} dq_x dq_y G_{\psi_\perp}^2(q_x,q_y)\frac{e^{-|z|\sqrt{q_x^2+q_y^2+\kappa^2}}}{\sqrt{q_x^2+q_y^2+\kappa^2}}. \tag{20}$$

Finally, by placing Eq. (11) into Eq. (20), evaluating the integral, and defining $N = N_x^4 N_y^4\pi^2/8^2$, an analytical and simple real-space expression for the effective potential can be obtained:

$$V_{\text{eff}}(z,\kappa,l) = N\frac{e^2}{4\pi\epsilon\epsilon_0}\left[\frac{e^{-|z|\sqrt{8l^2+\kappa^2}}}{\sqrt{8l^2+\kappa^2}}\right]. \tag{21}$$

Some features of this effective potential are discussed further below.

B. The *x*-*y* plane solution

To deal with the transversal contribution, we have solved the Schrödinger equation for Eq. (4) by using the well-known procedure described in Ref. [32]. For the x coordinate, the Schrödinger equation reads

$$-\frac{\hbar^2}{2m_e^*}\frac{d\psi_{\perp_x}}{dx^2} + V_{\text{e-w}}\psi_{\perp_x} = E\psi_{\perp_x}, \tag{22}$$

with $V_{\text{e-w}}$ being the electron-wall potential, associated with the GaAs structure embedded in the barriers as

$$V_{\text{e-w}} = 0.65[E_{\text{gap}}(\text{Al}_x\text{Ga}_{1-x}\text{As}) - E_{\text{gap}}(\text{GaAs})], \tag{23}$$

where the band gap energy for the barrier, considered to have infinite length, is given by [33]

$$E_{\text{gap}}(\text{Al}_x\text{Ga}_{1-x}\text{As}) = (1.424+1.247x)\,\text{eV}, \quad x<0.45, \tag{24}$$

and the band gap of the semiconductor nanostructure, dependent on the temperature T and the Al concentration x, is calculated from

$$E_{\text{gap}}(\text{GaAs}) = 1.519 - \frac{5.405\times10^{-4}T^2x}{T+207}\,\text{eV}. \tag{25}$$

We consider a typical Al concentration of $x = 0.23$ and a temperature of $T = 300K$. With these parameters, $V_{\text{e-w}} =$ 187 meV outside and 0 meV inside the GaAs structure. Thus, for a very small cross-section size, the electrons inside the GaAs can tunnel into the AlGaAs matrix. Additional values that were considered are as follows: $\epsilon_{r(\text{GaAs})} = 12.9$, $m^*_{e(\text{GaAs})} = 0.0665m_e$, with m_e being the electron mass, $\epsilon_{r(\text{AlGaAs})} = 12.247$, and $m^*_{e(\text{AlGaAs})} = 0.0857m_e$. As the difference of the dielectric constants between GaAs and AlGaAs is very small, the correction due to the dielectric discontinuity is not considered at this time. By solving Eq. (22), secular equations for the odd and even solutions are obtained:

$$\frac{l}{l_v}\tan\left[-l\frac{L_j}{2}\right] = M, \tag{26}$$

$$-M\cot\left[-l\frac{L_j}{2}\right] = \frac{l_v}{l}, \tag{27}$$

where $l_v \equiv \sqrt{\frac{2m^*_{e(\text{GaAs})}}{\hbar}(V_{\text{e-w}}-E_{n\text{-}j})}$, $M \equiv \frac{m^*_{e(\text{GaAs})}}{m^*_{e(\text{AlGaAs})}}$, l is defined as in Eq. (9), and $n = 0, 1, 2, \ldots$ is the quantum number. A similar procedure was followed for the y coordinate. Then, the ground-state energy $E_{x,y}$ can be calculated from the first interception in the graphical solution of Eq. (26), and once $E_{x,y}$ is known, l can be finally calculated and incorporated into the effective potential, Eq. (21).

C. Remarks on the effective potential

The effective potential described in Eq. (21) is a practical, real-space representation of the many-body interactions that govern the available quantum states of electrons under severe confinement. It implicitly contains the quantum confinement produced in all three spatial directions. In addition, this potential is able to incorporate the electronic population via a simple screening parameter κ for any experimental doping level. Values for κ used in this study and its corresponding electron

TABLE I. Nomenclature and equivalences of the screening parameters κ, electronic densities n, and n-type doping levels used in the calculations of this work.

κ label	κ value nm^{-1}	n label	n value (e/cm^3)	doping level
κ_1	0.5	n_1	10^{17}	Typical value used in devices
κ_2	1	n_2	10^{18}	Typical value used in devices
κ_3	10	n_3	10^{20}	High
κ_4	500	n_4	10^{23}	High
κ_5	5000	n_5	10^{25}	Experimentally unachievable

densities (n-type doping level in semiconductor materials) are presented in Table I.

Some other special characteristics of the effective potential must be highlighted. First, in clear contrast to the simple Yukawa model reported in [25], in Eq. (21) the confinement associated with the transversal x-y cross section is implicitly contained in the parameter l via its connection with the eigenenergies $E_{0\text{-}j}$ [see Eq. (9)]. As discussed further below, the transverse component plays a quite important role in the electronic distribution of nanometric cross-sectional structures.

Second, instead of the screening parameter κ of the simple Yukawa potential in Eq. (2), the effective screening in Eq. (21) has the more complex form $\sqrt{8l^2+\kappa^2}$, which implies that the x-y confinement contributes to V_{eff} (via the parameter l) in a way similar to the electronic density (via the parameter κ). Even more, the confinement and the electronic density have roughly similar weights in V_{eff}. That is, if the x-y cross section is small enough to establish a large $E_{x,y}$ value, then its screening contribution will be comparable in magnitude to a moderated value of κ. The latter can be clearly observed in Fig. 2(a), where the effective potential V_{eff} is plotted as a function of the e-e separation for two low electronic densities (n_1 and n_2) and three $L_{x,y}$ cross sections (8, 30, and 60 nm). As can be observed, when the confinement is strong enough, the magnitude of its influence on V_{eff} is similar to the screening effect of a low n value. For example, the magnitude of V_{eff} for n_1 with $L_{x,y} = 60$nm is quite similar to n_1 with $L_{x,y} = 30$ nm. This is a remarkable quality of V_{eff} that correctly indicates that the electronic distribution in the nanostructures is determined by a competition between the spatial confinement and the electronic density.

Third, in contrast to a Yukawa-like or bare Coulombic potential, V_{eff} does not present $1/r$ dependence. Instead, V_{eff} is proportional to $1/\sqrt{8l^2+\kappa^2}$. That is, in V_{eff} the usual dependence of the electrostatic potentials on the charges' separation has been replaced by an alternative and equivalent description, which explicitly takes into account the electronic density and the confinement in all three spatial directions.

To highlight the differences between V_{eff} and V_Y, in Fig. 2(b) both potentials are plotted as a function of the e-e separation. As expected, both potentials go to zero at large e-e separations. However, for e-e separations shorter than ∼10 nm considerable differences can be appreciated. In

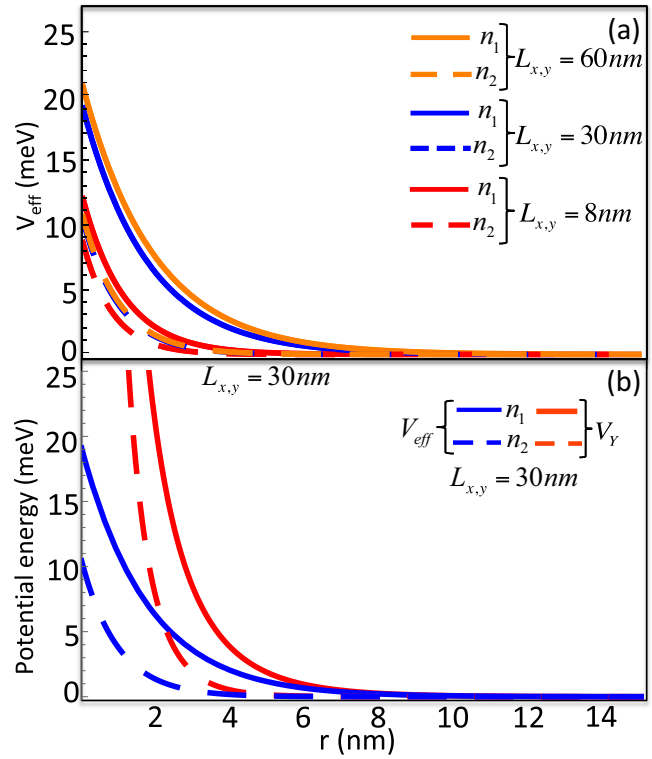

FIG. 2. Effective electron-electron interaction, Eq. (21), as a function of the electron's separation for (a) cross sections of sides $L_{x,y} = 8$, 30, and 60 nm and electronic densities n_1 (solid lines) and n_2 (dashed lines) and (b) electronic densities n_1 and n_2 and a cross section of side $L_{x,y} = 30$ nm. In (b), the Yukawa potential [Eq. (2); solid lines] is also shown.

contrast to the Yukawa or the pure Coulomb potential, V_{eff} does not diverge as the e-e separation goes to zero. Instead, the effective potential converges to a finite value of the order of tens of meV (which is larger for lower values of n). This effect is, of course, associated with the electronic screening effect.

III. ELECTRONIC DISTRIBUTION

A. Longitudinal confinement

One of the main features of the system that can be studied with our model is the electronic distribution inside the nanostructures. Hereafter, we explore this distribution in the various regimes of confinement imposed by $L_{x,y}$ and L_z. At first, we use $L_{x,y} = 1\,\mu$m to focus on the confinement in the z direction. Then, with $L_z = 30$ nm and $L_z = 1\,\mu$m, the electronic distributions in a quantum well (QW) and a bulk material, respectively, are considered. The charge distributions for the two test electrons are displayed in Figs. 3 and 4, respectively, where the results for both the effective and Yukawa potentials are plotted for comparison purposes.

As observed, at the higher electronic concentration (n_5), due to the strong electrostatic screening, only a central distribution is formed for both potentials and both systems [Figs. 3(e) and 4(e)]. For typical electronic concentrations, clear differences can be observed in the electronic distributions associated with V_Y and V_{eff} for the case of the QW, while

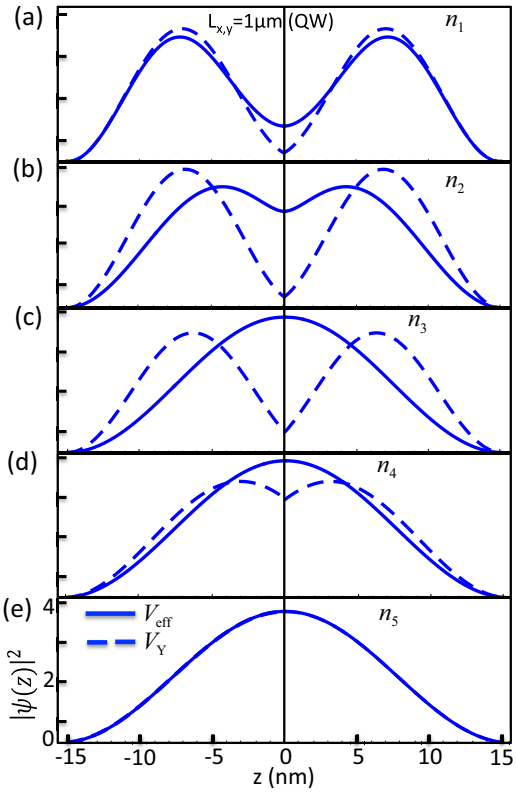

FIG. 3. Ground-state probability densities for a quantum well, $L_{x,y} = 1\,\mu$m and $L_z = 30$ nm. The results for the effective (solid lines) and the Yukawa (dashed lines) potentials are plotted for different electronic concentrations (see Table I).

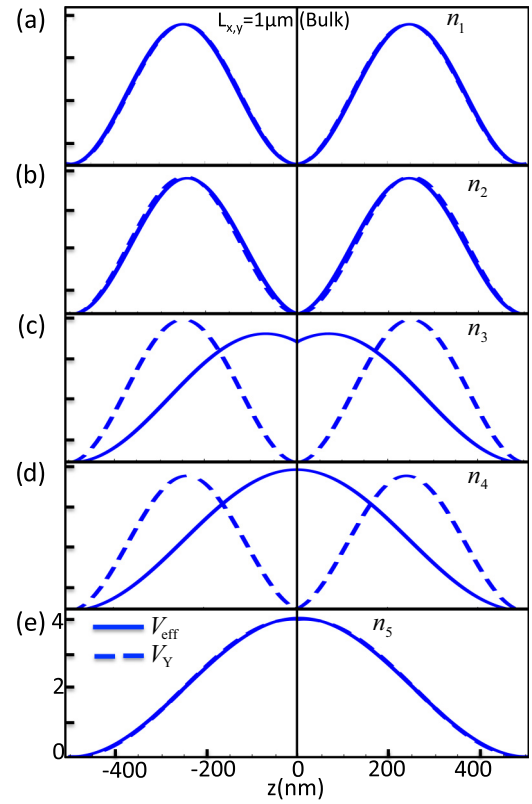

FIG. 4. Ground-state probability densities for a quasibulk material, $L_{x,y} = 1\,\mu$m and $L_z = 1\,\mu$m. The results for the effective (solid lines) and the Yukawa (dashed lines) potentials are plotted for different electronic concentrations (see Table I).

for the bulk both potentials have the same form [Figs. 3(a)–3(d) and 4(a)–4(d)]. In this case, the mismatching of the electronic distributions between potentials can be directly associated with the quantum confinement contribution of the transversal component (which is contained only in $V_{\rm eff}$). Even when the electronic distributions are clearly different for V_Y and $V_{\rm eff}$, the general trend is quite similar. The latter is due to the very weak x-y confinement ($L_{x,y} = 1\,\mu$m). As described further below, this is no longer the case when a strong x-y confinement is considered.

B. Transverse and longitudinal confinement

To help clarify the x-y transversal confinement sensibility of $V_{\rm eff}$, cross sections of size $L_{x,y} = 1\,\mu$m, 30 nm, and 8 nm are now considered. In Figs. 5 and 6 such distributions are presented. With the choice of these parameters, the electronic distribution associated with different low-dimensional structures can be studied: QWs [Fig. 5(a)], quantum dots (QDs) [Figs. 5(b) and 5(c)], QWRs [Figs. 6(b) and 6(c)], and a weakly confined quasibulk material [Fig. 6(a)]. Since the x-y confinement does not have any influence on V_Y, in this case only $V_{\rm eff}$ is discussed. Vertical dashed lines in Figs. 5 and 6 are an aid to the eye to identify the possible formation of a Wigner molecule, that is, if two independent electronic distribution peaks become well separated and centered at $\pm$L/4 [15,17–19].

As is evident in Figs. 5 and 6, the cross-section size greatly affects the electronic distribution for both $L_z = 30$ nm and $1\,\mu$m. Analogously to Figs. 3 and 4, for the highest (n_5) electronic concentration, a unique central distribution was obtained in all cases (data not shown). The same effect is observed for n_4 and n_3 when $L_z = 30$ nm (Fig. 5) and for

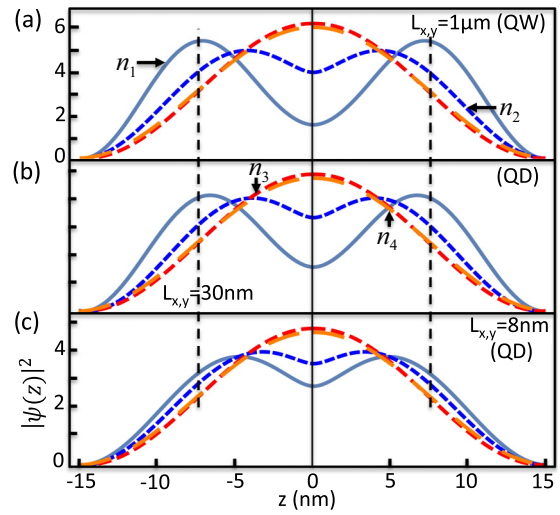

FIG. 5. Ground-state probability densities, calculated using the effective potential, Eq. (21), for $L_z = 30$ nm.

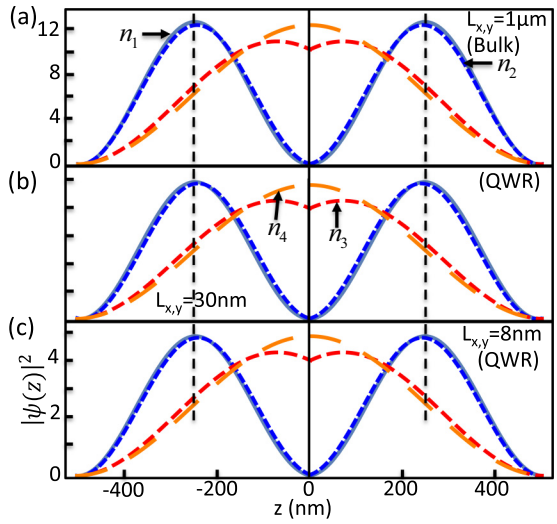

FIG. 6. Ground-state probability densities, calculated using the effective potential, Eq. (21), for $L_z = 1\,\mu$m.

n_4 when $L_z = 1\,\mu$m (Fig. 6). However, for $L_z = 1\,\mu$m and $n = n_3$, the electronic screening becomes weak enough to promote a twofold distribution. For lower n concentrations, the two-peak distribution becomes the dominant feature.

Interestingly, for typical electronic concentrations in doped semiconductors (n_1 and n_2), the electronic distribution predicted by V_{eff} follows a particular behavior for each kind of nanostructure. For example, for quantum dots [Figs. 5(b) and 5(c)], even when the distribution is almost identical for n_1, the two peaks become closer for the smallest $L_{x,y}$ value. In contrast, for QWRs [see Figs. 6(b) and 6(c)], even when the electronic distributions are also virtually identical for n_1 and n_2, the peaks' positions stay at $\pm L/4$ for both $L_{x,y} = 8$ and 30 nm. The latter behavior, directly related to the formation of a Wigner molecule, is discussed in Sec. IV. Finally, when larger $L_{x,y}$ values of 30 nm and 1 μm are considered, the n_1 and n_2 distributions no longer perfectly overlap each other [see Fig. 5(a)]. For the bulk material in Fig. 6(a), one can observe that the two well-defined equidistant peaks remain. Thus, for QWRs the model is able to describe the conditions for the formation of a Wigner molecule.

From the results discussed before, it is clear that by incorporating the carrier confinement in all three spatial directions, V_{eff} allows us to get a more complete description of the electronic distribution in a variety of nanostructures and doping levels. In the next section, we contrast V_{eff} with available experimental data related to the formation of a Wigner molecule in QWRs, which is especially interesting because it involves the two main ingredients of this contribution: many-electron interaction and a specific kind of geometrical restriction. In particular, the experimental results will allow us to assess the accuracy of the effective potential in predicting, at low computational cost, the conditions for the Wigner crystallization.

IV. WIGNER CRYSTALLIZATION: EXPERIMENTAL COMPARISON

In Fig. 7, the relative position of the maximum of the electronic distribution in one half of the z axis, calculated with

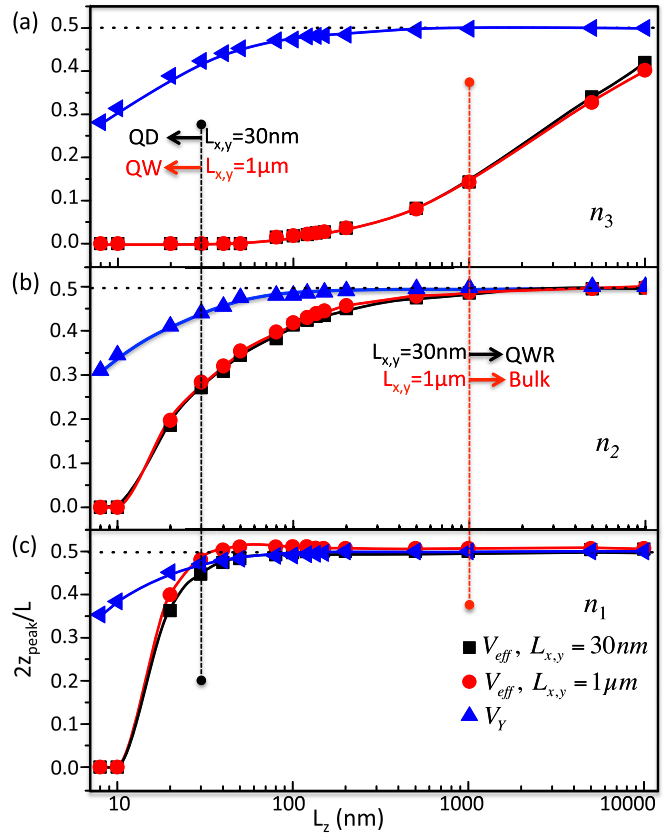

FIG. 7. Peak position, $2z_{\text{peak}}/L$, for the ground-state electronic distribution for $L_{x,y} = 30$ nm (black squares), $L_{x,y} = 1\,\mu$m (red circles), and three electronic densities: (a) n_3, (b) n_2, and (c) n_1 (see Table I). The horizontal dotted lines stand for the condition of the Wigner crystallization. The vertical dotted lines help to define the transition between the kinds of structures defined by the combination of $L_{x,y}$ and L_z.

V_Y and V_{eff} for three electronic concentrations, is displayed. The horizontal dashed line at 0.5 establishes the condition for the Wigner crystal formation; that is, it helps us to visualize when two equidistant well-defined peaks at the center of each half of the distribution are formed.

As noted in Fig. 7, the formation of the Wigner molecule strongly depends on the dimensionality of the structure and its electronic concentration. Unlike the Yukawa potential, in which the Wigner molecule was always found for QWRs at low electronic concentrations [25], the effective potential predicts a more intricate behavior: (i) for high electronic concentrations ($n > 10^{20}\,e/\text{cm}^{-3}$), the Wigner molecule formation is not promoted at all [Fig. 7(a)], and (ii) for systems with typical extrinsic n-doping levels ($10^{17}\,e/\text{cm}^3 < n < 10^{20}\,e/\text{cm}^3$), the Wigner molecule can be formed for $L_z \gtrsim 40$ nm and $n = n_1$ or, alternatively, for a large $L_z > 100$ nm and $n = n_2$ [see Fig. 7(b)]. It is worth stressing that all these characteristics are qualitatively consistent with experimental observations and early theoretical works on the Wigner crystallization [13–15,17–19].

Finally, in Fig. 8, the predictions based on the effective potential are compared with data from experimental reports that confirm the existence of the Wigner molecule [13,14].

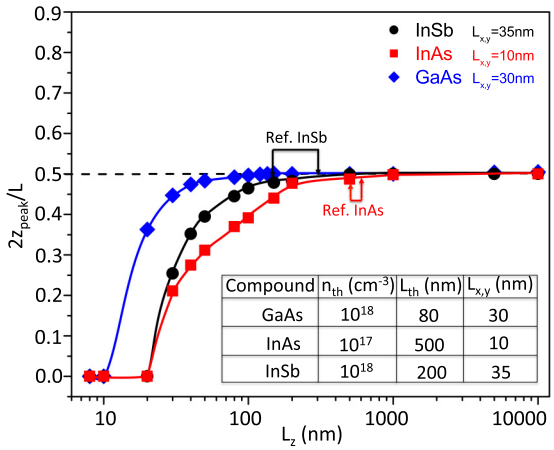

Compound	n_{th} (cm^{-3})	L_{th} (nm)	$L_{x,y}$ (nm)
GaAs	10^{18}	80	30
InAs	10^{17}	500	10
InSb	10^{18}	200	35

FIG. 8. Relative peak position, $2z_{peak}/L$, for the ground-state electronic distribution predicted by the effective potential, Eq. (21). Results for InSb with $L_{x,y} = 35$ nm (circles), InAs with $L_{x,y} = 10$ nm (squares), and GaAs with $L_{x,y} = 30$ nm (diamonds). QWRs are presented as a function of the wire length. The inset lists the n and L threshold values, predicted by V_{eff}, for the formation of a Wigner molecule.

Material parameters were modified to match the experimental InSb and InAs semiconductor QWRs. The systems considered were an InSb QWR of cross section $L_{x,y} = 35$ nm, embedded in an InAs matrix [13], and an InAs QWR, with $L_{x,y} = 10$ nm and electronic density $n_{\text{InAs}} = 10^{17}\,\text{cm}^{-3}$, embedded in a Si matrix [14].

Experimental tunneling spectroscopy measurements of electronic localized states in the InSb QWRs showed the onset of a Wigner molecule at $L_z = 160$ nm and a theoretical prediction of a complete formation of the Wigner molecule for a 300-nm-long QWR [13]. The results obtained by using V_{eff} agree remarkable well with the latter values, considering an electronic density of $10^{17}\,e/\text{cm}^3$, as depicted in Fig. 8. On the other hand, the local electronic transport by scanning gate microscopy measurements of the InAs QWRs, reported in Ref. [14], establish the formation of the Wigner molecule for L_z values between 500 and 600 nm, which also match very well with the values predicted by our effective potential model, as also observed in Fig. 8. The inset shows the n values predicted by V_{eff} for the critical concentration n_{th} and the threshold length ($L_z = L_{\text{th}}$) at which the Wigner molecule should appear in QWRs of different semiconductor materials. Experimental measurements in GaAs QWRs are currently in progress in order to explicitly compare with the theoretical predictions.

V. CONCLUDING REMARKS

In summary, we have derived an analytical, real-space representation of an effective potential that is able to describe, at a low computational cost, the many-body effects on the electronic distribution in low-dimensional structures. This effective potential takes into account the electronic confinement in all three spatial dimensions and the *e-e* interaction via a Yukawa-like potential. The derived effective potential allows one to explore the effects of key parameters, such as size, chemical composition, and the n-type impurity level, on the electronic distribution of different kinds of nanostructures. We found that the effective potential predictions matched remarkably well experimental observations related to the Wigner crystallization in QWRs.

Further use of the effective potential in nanostructures of more complex geometries would shed light on both the formation and stability of other unique electronic distributions involving the many-body electronic interactions.

ACKNOWLEDGMENTS

The authors acknowledge financial support from Consejo Nacional de Ciencia y Tecnología (CONACyT; Grants No. FC2016-01/2408, No. CB2015-01/1257434, No. CB2014/237425, and No. CB2016-01/287067) and PRODEP (Grant No. 511-6/17-4023). R.C.-P. also acknowledges the financial support provided by the Marcos Moshinsky Foundation.

[1] X.-L. Wang, J. Appl. Phys. **99**, 121301 (2006).
[2] D. Bimberg and U. W. Pohl, Mater. Today **14**, 388 (2011).
[3] Z. Dong, Y. André, V. G. Dubrowskii, C. Bougerol, C. Leroux, M. R. Ramdani, G. Monier, A. Trassoudaine, D. Castelluci, and E. Gil, Nanotechnology **28**, 125602 (2017).
[4] E. Cruz-Hernández, S. Shimomura, and V. H. Méndez-García, Appl. Phys. Lett. **101**, 073112 (2012).
[5] Y. Xia, P. Yang, Y. Sun, Y. Wu, B. Mayers, B. Gates, Y. Yin, F. Kim, and H. Yan, Adv. Mater. **15**, 353 (2003).
[6] M. Fuechsle, S. Mahapatra, F. A. Zwanenburg, M. Friesen, M. A. Eriksson, and M. Y. Simmons, Nat. Nanotech. **5**, 502 (2010).
[7] X. Dai, Z. Zhang, Y. Jin, Y. Niu, H. Cao, X. Liang, L. Chen, J. Wang, and X. Peng, Nature (London) **515**, 96 (2014).
[8] Y. Oreg, G. Refael, and F. von Oppen, Phys. Rev. Lett. **105**, 177002 (2010).
[9] N. T. Ziani, F. Cavaliere, and M. Sassetti, New J. Phys. **15**, 063002 (2013).
[10] J. I. Climente, M. Royo, J. L. Movilla, and J. Planelles, Phys. Rev. B **79**, 161301(R) (2009).
[11] Y. Alhassid, Rev. Mod. Phys. **72**, 895 (2000).
[12] V. V. Deshpande and M. Bockrath, Nat. Phys. **4**, 314 (2008).
[13] L. H. Kristinsdóttir, J. C. Cremon, H. A. Nilsson, H. Q. Xu, L. Samuelson, H. Linke, A. Wacker, and S. M. Reimann (Nanometer Structure Consortium, nmC@LU), Phys. Rev. B **83**, 041101(R) (2011).
[14] A. A. Zhukov, C. Volk, A. Winden, H. Hardtdegen, and T. Schäpers, JETP Lett. **100**, 32 (2014).
[15] E. Wigner, Phys. Rev. **46**, 1002 (1934).
[16] S. A. Söffing, M. Bortz, I. Schneider, A. Struck, M. Fleischhauer, and S. Eggert, Phys. Rev. B **79**, 195114 (2009).
[17] J. S. Meyer and K. A. Matveev, J. Phys. Condens. Matter **21**, 023203 (2009).
[18] H. J. Schulz, Phys. Rev. Lett. **71**, 1864 (1993).

[19] J.-J. Wang, W. Li, S. Chen, Gao Xianlong, M. Rontani, and M. Polini, Phys. Rev. B **86**, 075110 (2012).
[20] G. Sun and T. Vekua, Phys. Rev. B **93**, 205137 (2016).
[21] J. Planelles, M. Royo, A. Ballester, and M. Pi, Phys. Rev. B **80**, 045324 (2009).
[22] F. Malet, A. Mirtschink, J. C. Cremon, S. M. Reimann, and P. Gori-Giorgi, Phys. Rev. B **87**, 115146 (2013).
[23] A. Ballester, J. M. Escartín, J. L. Movilla, M. Pi, and J. Planelles, Phys. Rev. B **82**, 115405 (2010).
[24] V. V. Ravi Kishore, B. Partoens, and F. M. Peeters, Phys. Rev. B. **82**, 235425 (2010).
[25] R. Méndez-Camacho, E. Cruz-Hernández, and R. Castañeda-Priego, Phys. Rev. B **95**, 085437 (2017).
[26] L. F. Rojas-Ochoa, R. Castañeda-Priego, V. Lobaskin, A. Stradner, F. Scheffold, and P. Schurtenberger, Phys. Rev. Lett. **100**, 178304 (2008).
[27] P. Debye and E. Hückel, Phys. Z. **24**, 185 (1923).
[28] E. Fermi, Rend. Accad. Naz. Lincei, **6**, 602 (1927); **7**, 726 (1928).
[29] L. H. Thomas, Proc. Cambridge Philos. Soc. **23**, 542 (1927).
[30] E. Stern, R. Wagner, F. J. Sogworth, R. Breaker, T. M. Fahmy, and M. A. Reed, Nano Lett. **7**, 3405 (2007).
[31] S. Bednarek, B. Szafran, T. Chwiej, and J. Adamowski, Phys. Rev. B. **68**, 045328 (2003).
[32] H. Paul, *Quantum Wells, Wires and Dots: Theoretical and Computational Physics of Semiconductor Nanostructures*, 2nd ed. (Wiley, West Sussex, United Kingdom, 2006).
[33] Y. P. Varshni, Physica **34**, 149 (1967).